Morphology and growth habit of a new flux-grown layered semiconductor $KBiS_2$ revealed by diffraction-contrast tomography

Kejian Qu,[†] Hrishikesh Bale,[‡] Zachary W. Riedel,[¶] Junehu Park,[¶] Leilei Yin,[§] André Schleife,[¶,‖] and Daniel P. Shoemaker[*,¶]

[†]*Department of Physics and Materials Research Laboratory, University of Illinois at Urbana-Champaign, Urbana, IL 61801*

[‡]*Carl Zeiss X-ray Microscopy, Inc. Pleasanton, CA 94588*

[¶]*Department of Materials Science and Engineering and Materials Research Laboratory, University of Illinois at Urbana-Champaign, Urbana, IL 61801*

[§]*Beckman Institute, University of Illinois at Urbana-Champaign, Urbana, IL 61801*

[‖]*National Center for Supercomputing Applications, University of Illinois at Urbana-Champaign, Urbana, IL 61801*

E-mail: dpshoema@illinois.edu

Abstract

Single crystals of rhombohedral $KBiS_2$ were synthesized for the first time, and the structure, growth habit and properties of this layered semiconductor are presented. The single crystals form from a reactive K_2S_5 salt flux and are still embedded in the residual flux, without removal from the reaction vessel throughout the whole study. Laboratory diffraction contrast tomography (LabDCT) is used to identify the crystalline phase, orientation, and microstructure of crystals. Meanwhile, powder and single crystal X-ray diffraction were performed to determine detailed crystallographic information. Morphology of the crystalline assemblies observed by absorption contrast tomography reveals screw-dislocation-driven growth to be the dominant mechanism. First-principles electronic structure simulations predict rhombohedral $KBiS_2$ to be a semiconductor with an indirect band gap, which was confirmed by experiment. This study demonstrates how non-destructive tomography imaging and 3D crystallography methods can lead to advances in discovering new materials and studying crystal growth mechanisms.

Introduction

The discovery of new inorganic materials is sustained by the growth of high-quality single crystals that enable robust characterization of their functional properties and permit structure solution from single-crystal diffraction. The most effective crystal growth occurs from liquids or gases, based on enigmatic growth mechanisms that are especially tantalizing in the grand challenge of obtaining metastable materials by extracting them from an aggressive growth medium. Reactions in molten fluxes can lead to such kinetically-trapped metastable phases unobtainable by direct combination of elements,[1] and these methods have proven to be prolific in producing new chalcogenide materials in particular.[2] These compounds are typically narrow-gap semiconductors and heavy elements lead to strong spin-orbit coupling, which can lead to topologically protected gaps, such as in $TlBiS_2$[3] and Bi_2Se_3.[4] Given the nascent field of crystal growth for nontrivial topology, the identification and high-quality growth of these materials is invaluable.

Unfortunately, the reaction vessels obscure the progression of phase nucleation, growth, and transformation. Some characterization of flux systems in-situ have provided a view of the crystallization and dissolution of phases in reactive fluxes, in particular by powder diffraction,[5,6] but these methods are poorly suited to probe growths with large crystals.

Here, using the case of a novel flux-grown layered semiconductor crystal, we show how a combination of high resolution X-ray absorption contrast tomography[7,8] and diffraction contrast tomography[9,10] can be applied to identify previously-undiscovered materials while simultaneously viewing the crystal morphology and growth habit. Since the Laue pattern indexation can be quickly checked against known crystal structures, a set of "unmatched" crystals was quickly identified, and the material was determined to be a new layered semiconductor $KBiS_2$, still embedded in the flux. Conducting the entire analysis non-destructively enables investigation of the crystals in their native environment while preserving the samples for further subsequent correlative characterization.

Understanding the growth of crystalline materials requires observing the growth habit and grain orientations. Traditional absorption X-ray tomography provides orientation indirectly by facets seen in density contrast.[11–13] Identifying crystalline phases and their orientations requires diffraction information, which is possible by additionally interrogating the Laue diffraction pattern during sample rotation, as embodied in X-ray diffraction contrast tomography (DCT).[14,15] And diffraction contrast tomography can be accomplished even with a laboratory X-ray source (LabDCT) instead of one of the few synchrotron sources.[16–18] While the DCT method has been used to map grain orientations (with resolutions around 50 µm) in Ti,[19,20] AlCu,[16] and Zn-Mg alloys,[21] with synchrotron and conventional X-ray tube sources, those studies are on freestanding materials with simple structures.

The utility of DCT for emerging materials, especially novel crystalline materials intact within their synthesis environment, has never been shown.

In this study, we take advantage of the grain visualization capabilities of DCT in combination with the wealth of single-crystal Laue diffraction data to confirm crystal size, shape, orientation and identity simultaneously on a much more complex sample. From absorption contrast tomography on the same sample, we identify needle and plate morphologies of rhombohedral $KBiS_2$ that can be attributed to different stages of nucleation and growth, suggesting a screw-dislocation-driven growth mechanism.[22] Applying these measurement techniques to future in-situ studies in extreme environments (especially in aggressive chemical potentials) will allow short-lived, kinetically-trapped phases to be obtained, which should accelerate the discovery of new metastable materials.

Experimental

Synthesis: The flux for $KBiS_2$ crystal growth is K_2S_5, which was synthesized by stoichiometric reaction of potassium (0.356 g, 99%) and sulfur (0.729 g, 99.9%). The potassium chunk was loaded into a one-side-open small quartz tube, which was loaded into a larger quartz tube with sulfur at the bottom to avoid direct contact between sulfur and potassium. The larger quartz tube was sealed under vacuum. After ramping up to 400 °C for 18 hours, the sample was kept at 400 °C for another 18 hours to allow sulfur to fully transport and react with potassium to form K_2S_5. Next, flux reactions were conducted in fused silica tubes with Bi shots (0.104 g, 99.9%, around $10\times2\times2$ mm^3) in K_2S_5 (0.236 g). The flux reactions contained a nominal stoichiometry of $2K_2S_5$ + Bi and were ramped to 600 °C in 6 hours, hold for 6 hours, then cooled to 300 °C in 50 hours, then quenched in water to ensure the remaining flux is amorphous.

Tomography: The sealed tubes were first examined by x-ray absorption contrast tomography using a Rigaku CTLab GX130 machine at Beckman Institute at University of Illinois to verify presence of crystals in the flux. High resolution absorption contrast tomography (ACT) and LabDCT measurements were carried out using the ZEISS Xradia 620 Versa X-ray microscope (Carl Zeiss X-ray Microscopy, Dublin CA). The objective based dual-magnification setup of the X-ray microscope allowed zooming into the interior region of interest at a higher resolution of 1 µm/voxel without the need for cutting samples to smaller sizes as would be needed on a conventional microCT setup. A full-field of view scan collected at 6 µm/voxel provides a full overview of the tube enabling to pinpoint local regions of interest for high resolution absorption and diffraction contrast tomography. For ACT, 1601 projections were obtained with a 3 s exposure at an X-ray energy of 160 kV at 10 W, using a HE2 high energy filter. The data was reconstructed using the microscope's proprietary 3D reconstruction software (ZEISS XMReconstructor) which is based on the FDK reconstruction algorithm. Diffraction contrast tomography was performed at 160 kV in the Laue focusing geometry where source and detector were aligned equidistant from the sample, see Figure S1 in Supporting Information.[23] A set of 181 diffraction projections were collected over 360 degree rotation of the sample, each with an exposure of 180 s. The interior region of interest for diffraction contrast tomography was determined from 3D reconstructed absorption contrast tomography data using a scout-and-zoom method. 3D crystallographic reconstruction was carried out in a dedicated 3D grain mapping software[16] accompanied with the microscope (GrainMapper3Dv3.0; Xnovo Technology ApS, Denmark). For indexation of the crystal structures, a refined crystal parameter file was imported based on XRD measurements of isolated crystals of rhombohedral $KBiS_2$. Overlay of the grain reconstruction and the absorption data and 3D visualization and analysis was performed in Dragonfly Pro software (Object Research Systems, Montreal Canada).

Crystal structure determination: Duplicate samples were made to obtain individual single crystals, using the same stoichiometry and heating sequence. Crystals were collected by dissolving the flux in distilled water. Single-crystal X-ray diffraction on a Bruker D8 Venture Duo gave a structure of $KBiS_2$, with the $TlBiS_2$ structure type in space group $R\bar{3}m$. Powder X-ray diffraction was performed to verify that the crystalline product is single phase. Stoichiometric starting ingredients ($4Bi + K_2S_5 + K_2S_3$), where K_2S_3 was synthesized in the same way as K_2S_5 with stoichiometric K and S, produced cubic $KBiS_2$. The full refinement results and structures are given in Table S1 and Figure S1 in Supporting Information.[23]

UV-vis-NIR measurement: UV-vis-NIR measurements were done for ground powder using Varian Cary 5G, at the Materials Research Laboratory at University of Illinois, and the reflectance vs. wavelength data was converted and linearly fitted with Tauc method.[24] R_∞ is the diffuse reflectance of the sample, and $F(R_\infty)$ is the Kubelka-Munk function defined as $F(R_\infty) = (1 - R_\infty)^2/2R_\infty$. In Tauc method, $(F(R_\infty) \cdot h\nu)^{1/2} = B(h\nu - E_\mathrm{g})$, where $h\nu = 1239.7/\lambda$ having the unit of eV, wavelength λ having the unit of nm and B being a constant. Finally, linear regression was performed for the linear portion of the $(F(R_\infty)\cdot h\nu)^{1/2}$ vs. energy $h\nu$ curve, and E_g is the intercept of the straight line with the horizontal axis, which is around 1.21 eV.

Band structure calculation: We used the Vienna Ab-Initio Simulation Package (VASP)[25–27] to compute the electronic structure and optical spectra within first-principles density functional theory (DFT). The generalized-gradient approximation by Perdew, Burke, and Ernzerhof (PBE)[28] was used to describe exchange and correlation and compared to the hybrid HSE06 functional by Heyd, Scuseria, and Ernzerhof.[29] The projector-augmented wave (PAW) method[30] was used to describe the electron-ion interaction and Kohn-Sham wave functions are expanded into a plane-wave basis up to a kinetic-energy cutoff of 500 eV. The spin-orbit interaction was taken into account in a fully non-collinear approach.[31] These simulations were performed for the atomic coordinates of the conventional cell provided by Materials Project (mpID 1223443)[32,33] that we converted to a primitive unit cell using AFLOW/ACONVASP.[34] We subsequently relaxed the atomic coordinates until all forces were less than 5 meV/Å. We used a $12 \times 12 \times 12$ Γ-centered $\mathbf{k}$-point grid for the Brillouin zone integration when computing the PBE electronic structure, a Gamma centered $4 \times 4 \times 4$ grid for the HSE06 data, and a Gamma centered $16 \times 16 \times 16$ grid for optical spectra.

Results and discussion

The flux reaction schematics and the crystal structure of rhombohedral $KBiS_2$, along with the tomography setup and both absorption contrast and diffraction contrast tomography data are all shown in Figure 1. Figure 1(a) shows the reaction schematic where Bi and K_2S_5 flux are loaded into a fused silica tube, shown in Figure 1(b). They reacted at 600°C and slow-cooled to 300°C. The tube has a 3 mm inner diameter and 1 mm wall thickness, as can be seen in Figure 1(e), typical of a single-crystal growth in reactive fluxes with moderate vapor pressures. The region used for tomography study is at the bottom portion of the

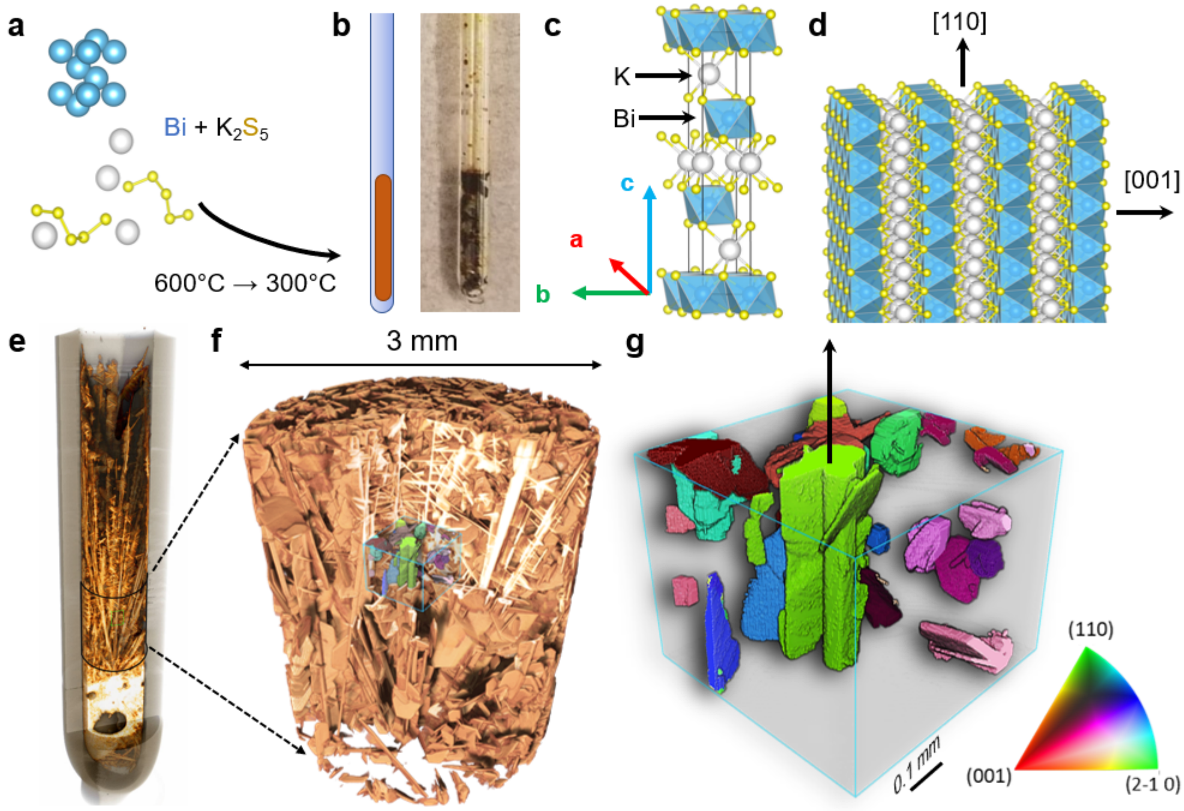

Figure 1: (a) Flux reaction schematics. Details of synthesis can be seen in Experimental Section. (b) Schematic and image of sample in quartz tube after reaction. The outer tube diameter is 5 mm. (c) Unit cell of rhombohedral $KBiS_2$. (d) [110] and [001] directions in layered rhombohedral $KBiS_2$ crystals. (e) Absorption contrast tomography of the sample, where the outside grey region is the glass tube with a wall thickness of 1 mm. A movie of the whole sample, including the glass tube, can be seen in Supporting Information. (f) Absorption contrast tomography corresponding to the region indicated in (e), with a portion cut to show the needle-shaped crystals. Another high-resolution scan movie in Supporting Information shows this region in detail. The central volume in color was used for diffraction tomography study. (g) LabDCT picture in inverse pole figure format with the largest central needle-shaped grain in [110] direction, indicated with the upward arrow.

tube, embedded in flux and is optically opaque. The unit cell of the crystalline product $KBiS_2$ is shown in Figure 1(c). The density-contrast reconstruction of the entire tube in the tomographic region is shown in Figure 1(f) with a density cutoff chosen so that only the Bi-containing crystals are visible, while the flux is transparent. Needle- and plate-shaped crystals with some dimensions greater than 1 mm are evident, and powder diffraction of replica samples, with all crystals ground together, confirmed they are the same phase (Figure S1).[23] Initially, no fit to the Laue patterns could be obtained by DCT using reported crystal structures of phases in the K–Bi–S system: $KBiS_2$,[35–38] KBi_3S_5,[39] $K_2Bi_8S_{13}$,[40] $KBi_{6.33}S_{10}$,[40] and $K_9Bi_{13}S_{24}$.[41] However, single-crystal diffraction data of crystals from a replica sample provided a structure solution of a new rhombohedral phase of $KBiS_2$, previously unreported in the Inorganic Crystal Structure Database (ICSD), which indexed the DCT Laue data with a high completeness value.[16] After our analysis was complete, this phase was also reported in powder form.[42]

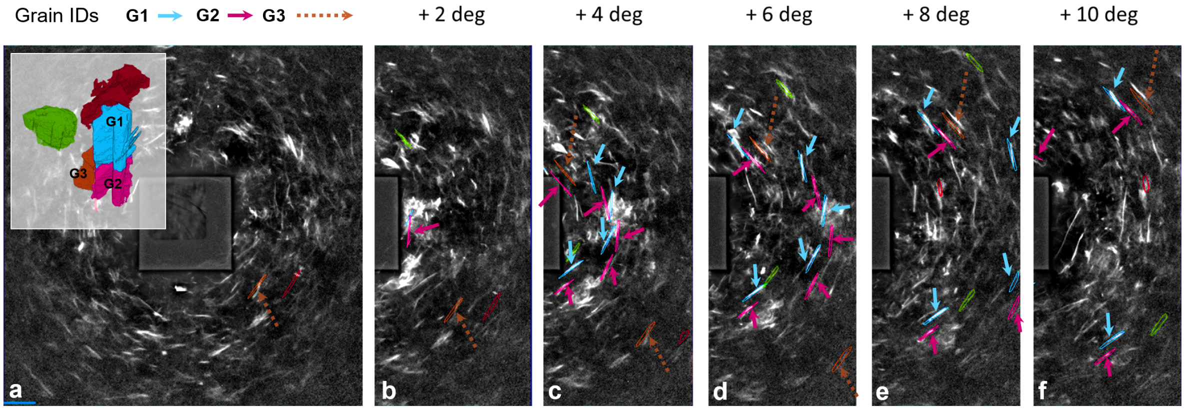

Figure 2: (a) Laue diffraction patterns collected from the region of interest indicated in Figure 1(f) and (g). For the sake of clarity, only 3 prominent grains and their corresponding Laue reflections are highlighted. (b-f) Selected Laue diffraction patterns are shown where the sample was rotated in 2° steps about the central axis of the glass tube. The outlined reflections correspond to the 3 grains with the colors assigned as unique identifiers. The tracking of reflections at the expected locations during sample rotation confirms the orientation determination. G1 and G2 have reflections that appear in the same frames because they are fragments of a much longer, crystallographically-aligned needle. A movie of raw Laue diffraction spots as the sample was rotated about its vertical axis (without background subtraction) is shown in Supporting Information.

Figure 1(g) shows the subset of crystals with which Laue patterns were obtained, colored with respect to their orientations based on the inverse pole figure (IPF) reference shown on the bottom right. The largest needle passing through the center of the volume has the (110) plane normal to the vertical direction and the most complete matching to the Laue pattern. We focus the bulk of our analysis on this grain. The orientation of the central needle-shaped grain is with the [110] direction upward, shown for the $KBiS_2$ structure in Figure 1(g).

Figure 2(a) shows raw diffraction patterns obtained in the DCT scan, where reflections from a large number of crystals are observed. Such large number of reflections is a result of the polychromatic X-ray diffraction from the entire illuminated cross-section of the sample, not just from the inner region of interest (the cube volume in Figure 1(g)). A diffuse background from the amorphous flux and glass wall was subtracted, but can be seen in the supplementary movie in Supporting Information.[23] Despite the presence of extraneous grains outside the region of interest, and the expected absorption of weak diffraction peaks by other grains or the tube wall, many strong reflections from the region of interest are successively tracked as the sample is rotated. Correct peak indexing is verified by tracking the diffraction spots from frame to frame, as the sample is rotated, shown in Figure 2(b-f). Two grains, G1 and G2, have reflections that precess as expected (marked as short arrows) as the sample is rotated by 10° over 5 frames. These reflections are primarily of {110} and {114} character, as indexed in Figure S3 in Supporting Information.[23] The ability to index the central grain, despite the presence of additional peaks and absorption from nearby grains, is a testament to the robustness of the grain reconstruction algorithm.[16] The grains G1 and G2 belong to a single needle with nominally the same crystal orientation as can be seen in Figure 1(g). High-resolution absorption contrast tomography images revealed that these long, needle-shaped crystals have occasional cross-sectional breaks along their length. The angular orientation sensitivity of DCT allows the detection of the subtle change in orientation at the breaks as distinct pairs of reflections, which is evident by the different locations of G1 and G2 reflections in Figure 2. Corresponding {hkl} and IPF indexations are shown in Figure S3, for a total of 26 grains indexed within the region of interest.[23]

We solved our unknown phase as rhombohedral $KBiS_2$, an ordered rocksalt-derived phase, in space group R$\bar{3}$m with $a = 4.12$ Å and $c = 22.09$ Å. This is in contrast with the established polymorph, cubic rocksalt $KBiS_2$,[35] with K^+ and Bi^{3+} randomly mixed and $a = 6.04$ Å. The rhombohedral phase has layered K and Bi (001) planes (Figure 1(d)), which correspond to (111) planes in the rocksalt structure. This type of rhombohedral R$\bar{3}$m ordering can also be seen in other ABQ_2 materials such as $AgSbTe_2$, in which both randomized NaCl type (Fm$\bar{3}$m) and ordered rhombohedral (R$\bar{3}$m) structures, together with other ordered structures, have been confirmed experimentally.[43,44]

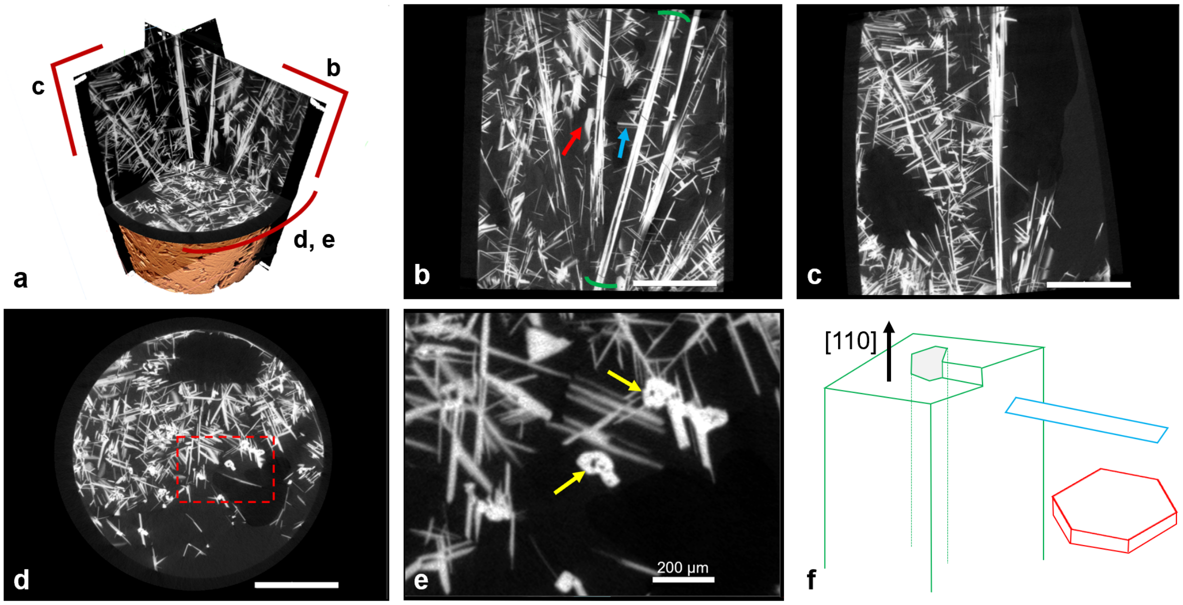

Figure 3: (a) 3D multi-planar view of the absorption contrast tomography data. (b-d) 2D planar views indicated in (a), where the bars all correspond to 1 mm. (e) Zoomed-in view of the red square region in (d) highlighting hollow channels in crystals with arrows. (f) Schematics of needle, plate, and dendrite, which are indicated in (b) with green arcs, red arrow, and blue arrow, respectively.

With the phase identified and orientation established, a few insights into the crystal growth mechanisms are apparent. Tomographic slices are viewed in absorption contrast mode in Figure 3, primarily focused on the long needles in the center of the sample, which, due to their unbroken lengths and protruding dendrites, can be assumed to be among the first large grains to form. Secondary and tertiary dendrites can be seen attached to the primary needle crystals that originate from the bottom of the reaction tube, with this convergence most apparent in Figure 3(b). The cross-sectional views of the needles in Figure 3(d) and (e) reveal hollow centers that likely arise from screw-dislocation-driven spiral growth[21,22] when the dislocation strain field energy is balanced by the creation of an internal surface energy.

Typically, screw-dislocation-driven growth will dominate when the supersaturation in the solution is relatively low,[45] which is observed here when the solution was in its initial period of slow cooling. From classical theory of dislocation-driven crystal growth,[46] the radius of the hollow channel r is related to the Burgers vector of dislocation b as $r = \frac{\mu b^2}{8\pi^2\gamma}$ where μ is the shear modulus, and γ is surface energy density. Here the Eshelby twist[47] is not included, since for this case, the outer radius of the needle-shaped crystals is significantly larger than the inner radius. The formula above indicates a comparatively small surface energy for this synthesis, since the crystal is grown from a polysulfide flux with similar composition.

The preferred [110] growth direction likely results from the easy addition of all three ions to this plane, rather than termination planes of a single ionic type, as would be the case for [001] (shown in Figure 1(d)). In this way, all ions can precipitate simultaneously. At the same time, the growth direction *inside the vessel* is aligned vertically–this insight is only possible by non-invasive tomography of the material inside the glass tube, while also revealing the interior pore structure of the grains.

Some plate-shaped crystals can also be seen, which is the result of layer-by-layer growth, when the supersaturation is in a moderate regime.[22,48] Finally, when the supersaturation further increases, especially in the late cooling period, dendrites will form. Overall, the screw-dislocation-driven growth dominated the initial period when the needles formed, and plates could only form starting from a later period, at which time there was not much empty space available. This is the reason why plate-shaped crystals larger than 1 mm × 0.5 mm are not observed, while the needle-shaped crystals in our tomography data are longer than 5 mm. Figure 3(f) shows the schematics of all three types of crystals.

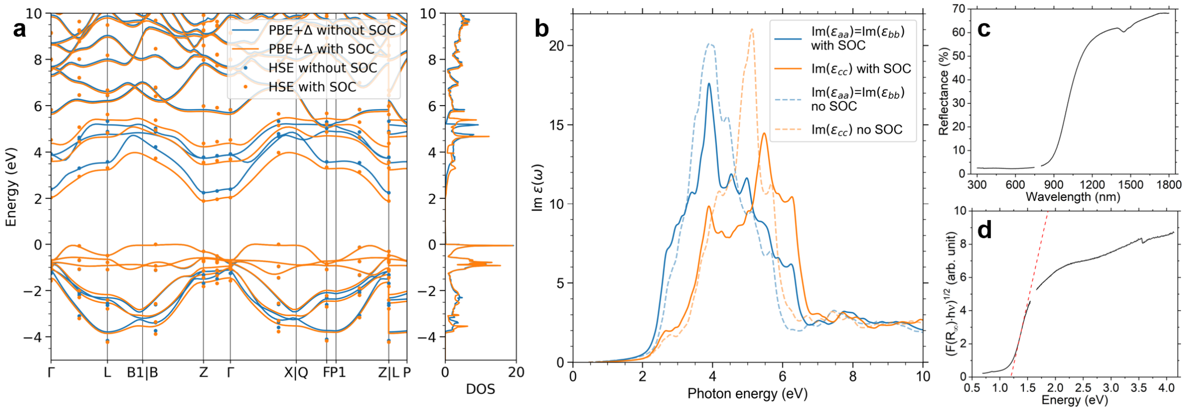

Figure 4: (a) Kohn-Sham electronic band structure (left) and density of states (right, in eV^{-1} normalized to 1 formula unit) from density functional theory simulations, with and without spin-orbit coupling. Results from the hybrid HSE06 exchange-correlation functional (dots) agree to within 0.5 eV with scissor-shifted (Δ=0.73 eV) PBE data (lines). (b) Calculated imaginary part of the frequency-dependent dielectric tensor. Scissor-shifted PBE data with (Δ=0.73 eV) and without (Δ=0.44 eV) spin-orbit coupling is compared, illustrating the influence of spin-orbit interaction on spectral shape, absorption onset, and anisotropy. (c) Experimental UV-vis-NIR diffuse reflectance measurement of powdered $KBiS_2$. (d) UV-vis-NIR data fit with the Tauc method, where Kubelka-Munk function $F(R_\infty)$ is defined in Experimental Section and the indirect band gap is 1.21 eV.

Finally, the electronic band structure of rhombohedral $KBiS_2$ is investigated by both theoretical calculation and ultraviolet-visible-near infrared (UV-vis-NIR) spectroscopy measurement, and the results are shown in Figure 4. Our Kohn-Sham electronic structure without spin-orbit coupling (SOC), shown in Figure 4(a), agrees well with that reported in an earlier work.[42] In addition, we also quantify the influence of spin-orbit coupling and find that including this effect decreases the band gap by about 0.29 eV (DFT-PBE) and 0.36 eV (HSE06). Several of the lowest conduction bands are split by spin-orbit coupling, see Figure S4 and S5 in the Supporting Information.[23] The valence bands between 2 and 4 eV below the Fermi energy are also affected, but to a lesser extent. These splittings also impact the optical properties of the material, as shown in Fig 4(b). Overall, the material shows a pronounced optical anisotropy between the optical conductivities ϵ_{aa} and ϵ_{cc}, as expected for a layered compound. The aforementioned SOC-driven splitting leads to a spectral broadening of both ϵ components on the whole, judged by the total width of the peak from ~2-6 eV.

The influence of exchange and correlation is significant in this material, as witnessed by the band gap increase from 1.15 eV to 1.88 eV, when comparing the results from DFT-PBE versus HSE06. UV-vis-NIR spectroscopy was used to measure the band gap using powder of rhombohedral $KBiS_2$ from replica samples. A Tauc fit to the reflectance data in Figure 4(c) gives an indirect band gap of is 1.21 eV, shown in Figure 4(d). The slight discrepancy of measured band gap compared to the calculated ones is likely due to surface degradation degradation inherent to alkali sulfides in air.

The large crystals obtained here are notably isostructural with rhombohedral $TlBiS_2$. The latter is known to undergo topological phase transitions and its electronic structure can be tuned by strain,[49,50] temperature,[51] or Se doping on S sites[51] based on DFT calculations. Experiments have demonstrated the tuning of the band structure by temperature[52] and doping.[3,53] For rhombohedral $KBiS_2$, which has a moderate band gap, albeit indirect, the tuning of the band structure via the aforementioned factors is possible, including doping Tl on K sites, and introducing strain.

Conclusion

In conclusion, we have shown that DCT can be used to identify phases with previously unknown crystal structures, even within bulky reaction vessels, and it can be used to characterize grain orientations. Combining the phase identification of large crystals with their growth mechanisms should lead to future studies that can engineer the growth conditions, such as changing the temperature profile, the starting stoichiometry, etc. in order to obtain the preferred phase and/or morphology. All tomographic analysis was performed without a synchrotron X-ray source and without opening the fused silica tube, showing the possibility of further study on sensitive samples and in-situ measurements during the growth process over a prolonged experimental period. Single-crystal UV-vis-NIR spectroscopy measurements confirmed rhombohedral $KBiS_2$ to be a semiconductor with an indirect band gap of 1.21 eV, which is corroborated by first-principles calculations. The parallels between the topological insulator candidate $TlBiS_2$ and isostructural $KBiS_2$ can be investigated in detail with subsequent optimization of crystal growth.

Acknowledgement

This work was supported by the US Department of Energy, Basic Energy Sciences (grant No. DE-SC0013897) for Early Career Research. Characterization was performed at the Materials Research Laboratory and Beckman Institute at the University of Illinois. Computational work was supported by the Illinois Materials Research Science and Engineering Center through the National Science Foundation MRSEC program under NSF Award No. DMR-1720633. This work made use of the Illinois Campus Cluster, a computing resource that is operated by the Illinois Campus Cluster Program (ICCP) in conjunction with the National Center for Supercomputing Applications (NCSA) and which is supported by funds from the University of Illinois at Urbana-Champaign. This research is part of the Blue Waters sustained-petascale computing project, which is supported by the National Science Foundation (awards OCI-0725070 and ACI-1238993) and the state of Illinois. Blue Waters is a joint effort of the University of Illinois at Urbana-Champaign and its National Center for Supercomputing Applications.

Supporting Information Available

The following files are available free of charge.

- Tube-Overview: movie of the whole tube
- Crystal-Detail: movie of absorption contrast tomography region, Figure 1(f)
- Laue: movie of Laue diffraction which no background deduction

- Table S1: crystallographic information of rhombohedral $KBiS_2$ from single crystal XRD
- Figure S1: powder XRD and structure for both rhombohedral and cubic $KBiS_2$
- Figure S2: SEM and microscope pictures of rhombohedral $KBiS_2$ crystals
- Figure S3: Laue diffraction rotation tracking with {hkl} planes and crystal orientations
- Figure S4: DFT-PBE electronic band structure
- Figure S5: HSE06 electronic band structure

References

(1) Latturner, S. E. Clusters, Assemble: Growth of Intermetallic Compounds from Metal Flux Reactions. *Acc. Chem. Res.* **2018**, *51*, 40–48.

(2) Kanatzidis, M. G. Molten alkali-metal polychalcogenides as reagents and solvents for the synthesis of new chalcogenide materials. *Chem. Mater.* **1990**, *2*, 353–363.

(3) Sato, T.; Segawa, K.; Kosaka, K.; Souma, S.; Nakayama, K.; Eto, K.; Minami, T.; Ando, Y.; Takahashi, T. Unexpected mass acquisition of Dirac fermions at the quantum phase transition of a topological insulator. *Nat. Phys.* **2011**, *7*, 840–844.

(4) Bansal, N.; Kim, Y. S.; Edrey, E.; Brahlek, M.; Horibe, Y.; Iida, K.; Tanimura, M.; Li, G.-H.; Feng, T.; Lee, H.-D.; Gustafsson, T.; Andrei, E.; Oh, S. Epitaxial growth of topological insulator Bi2Se3 film on Si(111) with atomically sharp interface. *Thin Solid Films* **2011**, *520*, 224–229.

(5) Shoemaker, D. P.; Hu, Y.-J.; Chung, D. Y.; Halder, G. J.; Chupas, P. J.; Soderholm, L.; Mitchell, J. F.; Kanatzidis, M. G. In situ studies of a platform for metastable inorganic crystal growth and materials discovery. *Proc. Natl. Acad. Sci. U.S.A.* **2014**, *111*, 201406211.

(6) Moorhouse, S. J.; Wu, Y.; Buckley, H. C.; O'Hare, D. Time-resolved in situ powder X-ray diffraction reveals the mechanisms of molten salt synthesis. *Chem. Commun.* **2016**, *52*, 13865–13868.

(7) Stock, S. X-ray microtomography of materials. *Int. Mater. Rev.* **1999**, *44*, 141–164.

(8) Stock, S. R. Recent advances in X-ray microtomography applied to materials. *Int. Mater. Rev.* **2008**, *53*, 129–181.

(9) Ludwig, W.; Schmidt, S.; Lauridsen, E. M.; Poulsen, H. F. X-ray diffraction contrast tomography: a novel technique for three-dimensional grain mapping of polycrystals. I. Direct beam case. *J. Appl. Crystallogr.* **2008**, *41*, 302–309.

(10) Johnson, G.; King, A.; Honnicke, M. G.; Marrow, J.; Ludwig, W. X-ray diffraction contrast tomography: a novel technique for three-dimensional grain mapping of polycrystals. II. The combined case. *J. Appl. Crystallogr.* **2008**, *41*, 310–318.

(11) Maire, E.; Withers, P. J. Quantitative X-ray tomography. *Int. Mater. Rev.* **2014**, *59*, 1–43.

(12) Salvo, L.; Cloetens, P.; Maire, E.; Zabler, S.; Blandin, J.; Buffière, J.; Ludwig, W.; Boller, E.; Bellet, D.; Josserond, C. X-ray micro-tomography an attractive characterisation technique in materials science. *Nucl. Instrum. Methods B.* **2003**, *200*, 273 – 286, Proceedings of the E-MRS 2002 Symposium I on Synchrotron Radiation and Materials Science.

(13) Baruchel, J.; Di Michiel, M.; Lafford, T.; Lhuissier, P.; Meyssonnier, J.; Nguyen-Thi, H.; Philip, A.; Pernot, P.; Salvo, L.; Scheel, M. Synchrotron X-ray imaging for crystal growth studies. *Compt. Rend. Phys.* **2013**, *14*, 208 – 220.

(14) Shahani, A. J.; Xiao, X.; Lauridsen, E. M.; Voorhees, P. W. Characterization of metals in four dimensions. *Mater. Res. Lett.* **2020**, *8*, 462–476.

(15) Ludwig, W.; Reischig, P.; King, A.; Herbig, M.; Lauridsen, E. M.; Johnson, G.; Marrow, T. J.; Buffière, J. Y. Three-dimensional grain mapping by x-ray diffraction contrast tomography and the use of Friedel pairs in diffraction data analysis. *Rev. Sci. Instrum.* **2009**, *80*, 033905.

(16) Bachmann, F.; Bale, H.; Gueninchault, N.; Holzner, C.; Lauridsen, E. M. 3D grain reconstruction from laboratory diffraction contrast tomography. *J. Appl. Crystallogr* **2019**, *52*, 643–651.

(17) Holzner, C.; Lavery, L.; Bale, H.; Merkle, A.; McDonald, S.; Withers, P.; Zhang, Y.; Jensen, D. J.; Kimura, M.; Lyckegaard, A.; et al., Diffraction Contrast Tomography in the Laboratory – Applications and Future Directions. *Microscopy Today* **2016**, *24*, 34–43.

(18) Oddershede, J.; Sun, J.; Gueninchault, N.; Bachmann, F.; Bale, H.; Holzner, C.; Lauridsen, E. Non-destructive Characterization of Polycrystalline Materials in 3D by Laboratory Diffraction Contrast Tomography. *Integr. Mater. Manuf. Innov.* **2019**, *8*, 217–225.

(19) Ludwig, W.; King, A.; Reischig, P.; Herbig, M.; Lauridsen, E.; Schmidt, S.; Proudhon, H.; Forest, S.; Cloetens, P.; du Roscoat, S. R.; Buffière, J.; Marrow, T.; Poulsen, H. New opportunities for 3D materials science of polycrystalline materials at the micrometre lengthscale by combined use of X-ray diffraction and X-ray imaging. *Mater. Sci. Eng. A* **2009**, *524*, 69 – 76.

(20) Ludwig, W.; King, A.; Herbig, M.; Reischig, P.; Marrow, J.; Babout, L.; Lauridsen, E. M.; Proudhon, H.; Buffière, J. Y. Characterization of polycrystalline materials using synchrotron X-ray imaging and diffraction techniques. *JOM* **2010**, *62*, 22–28.

(21) Moniri, S.; Bale, H.; Volkenandt, T.; Wang, Y.; Gao, J.; Lu, T.; Sun, K.; Ritchie, R. O.; Shahani, A. J. Multi-Step Crystallization of Self-Organized Spiral Eutectics. *Small* **2020**, *16*, 1906146.

(22) Meng, F.; Morin, S. A.; Forticaux, A.; Jin, S. Screw Dislocation Driven Growth of Nanomaterials. *Acc. Chem. Res.* **2013**, *46*, 1616–1626.

(23) Supporting Information available online.

(24) Makuła, P.; Pacia, M.; Macyk, W. How To Correctly Determine the Band Gap Energy of Modified Semiconductor Photocatalysts Based on UV–Vis Spectra. *J. Phys. Chem. Lett.* **2018**, *9*, 6814–6817.

(25) Kresse, G.; Joubert, D. From ultrasoft pseudopotentials to the projector augmented-wave method. *Phys. Rev. B* **1999**, *59*, 1758–1775.

(26) Kresse, G.; Furthmüller, J. Efficient iterative schemes for ab initio total-energy calculations using a plane-wave basis set. *Phys. Rev. B* **1996**, *54*, 11169–11186.

(27) Gajdoš, M.; Hummer, K.; Kresse, G.; Furthmüller, J.; Bechstedt, F. Linear optical properties in the projector-augmented wave methodology. *Phys. Rev. B* **2006**, *73*, 045112.

(28) Perdew, J. P.; Burke, K.; Ernzerhof, M. Generalized Gradient Approximation Made Simple. *Phys. Rev. Lett.* **1996**, *77*, 3865–3868.

(29) Heyd, J.; Scuseria, G. E.; Ernzerhof, M. Erratum: "Hybrid functionals based on a screened Coulomb potential" [J. Chem. Phys. **118**, 8207 (2003)]. *J. Chem. Phys.* **2006**, *124*, 219906.

(30) Blöchl, P. E. Projector augmented-wave method. *Phys. Rev. B* **1994**, *50*, 17953–17979.

(31) Steiner, S.; Khmelevskyi, S.; Marsmann, M.; Kresse, G. Calculation of the magnetic anisotropy with projected-augmented-wave methodology and the case study of disordered $Fe_{1-x}Co_x$ alloys. *Phys. Rev. B* **2016**, *93*, 224425.

(32) Jain, A.; Ong, S. P.; Hautier, G.; Chen, W.; Richards, W. D.; Dacek, S.; Cholia, S.; Gunter, D.; Skinner, D.; Ceder, G.; Persson, K. a. The Materials Project: A materials genome approach to accelerating materials innovation. *APL Mater.* **2013**, *1*, 011002.

(33) Ong, S. P.; Richards, W. D.; Jain, A.; Hautier, G.; Kocher, M.; Cholia, S.; Gunter, D.; Chevrier, V. L.; Persson, K. A.; Ceder, G. Python Materials Genomics (pymatgen): A robust, open-source python library for materials analysis. *Comput. Mater. Sci.* **2013**, *68*, 314–319.

(34) Setyawan, W.; Curtarolo, S. High-throughput electronic band structure calculations: Challenges and tools. *Comput. Mater. Sci.* **2010**, *49*, 299–312.

(35) Boon, J. W. The crystal structure of NaBiS2 and KBiS2. *Rec. Trav. Chim. Pays-Bas* **1944**, *63*, 32–34.

(36) Rosales, B. A.; White, M. A.; Vela, J. Solution-Grown Sodium Bismuth Dichalcogenides: Toward Earth-Abundant, Biocompatible Semiconductors. *J. Am. Chem. Soc.* **2018**, *140*, 3736–3742.

(37) Yang, C.; Wang, Z.; Wu, Y.; Lv, Y.; Zhou, B.; Zhang, W.-H. Synthesis, Characterization, and Photodetector Application of Alkali Metal Bismuth Chalcogenide Nanocrystals. *ACS Appl. Energy Mater.* **2019**, *2*, 182–186.

(38) Glemser, O.; Filcek, M. Über Alkalithiowismutate(III). *Z. Anorg. Allg. Chem.* **1955**, *279*, 321–323.

(39) McCarthy, T. J.; Tanzer, T. A.; Kanatzidis, M. G. A New Metastable Three-Dimensional Bismuth Sulfide with Large Tunnels: Synthesis, Structural Characterization, Ion-Exchange Properties, and Reactivity of KBi3S5. *J. Am. Chem. Soc. 117*.

(40) Kanatzidis, M. G.; McCarthy, T. J.; Tanzer, T. A.; Chen, L.-H.; Iordanidis, L.; Hogan, T.; Kannewurf, C. R.; Uher, C.; Chen, B. Synthesis and Thermoelectric Properties of the New Ternary Bismuth Sulfides KBi6.33S10 and K2Bi8S13. *Chem. Mater.* **1996**, *8*, 1465–1474.

(41) Davaasuren, B.; Alahmari, F.; Dashjav, E.; Khanderi, J.; Rothenberger, A. Synthesis and Characterization of the Ternary Thiobismuthates A9Bi13S24 (A = K, Rb). *Z. Anorg. Allg. Chem.* **2016**, *642*, 1480–1485.

(42) McClain, R.; Malliakas, C. D.; Shen, J.; He, J.; Wolverton, C.; González, G. B.; Kanatzidis, M. G. Mechanistic insight of KBiQ $_2$ (Q = S, Se) using panoramic synthesis towards synthesis-by-design. *Chem. Sci.* **2021**, *12*, 1378–1391.

(43) Hoang, K.; Mahanti, S. D. Atomic and electronic structures of I-V-VI2 ternary chalcogenides. *J. Sci. Adv. Mater. Dev.* **2016**, *1*, 51 – 56.

(44) Quarez, E.; Hsu, K.-F.; Pcionek, R.; Frangis, N.; Polychroniadis, E. K.; Kanatzidis, M. G. Nanostructuring, Compositional Fluctuations, and Atomic Ordering in the Thermoelectric Materials AgPbmSbTe2+m. The Myth of Solid Solutions. *J. Am. Chem. Soc.* **2005**, *127*, 9177–9190.

(45) Morin, S. A.; Bierman, M. J.; Tong, J.; Jin, S. Mechanism and Kinetics of Spontaneous Nanotube Growth Driven by Screw Dislocations. *Science* **2010**, *328*, 476–480.

(46) Frank, F. C. Capillary equilibria of dislocated crystals. *Acta Crystallogr.* **1951**, *4*, 497–501.

(47) Eshelby, J. D. Screw Dislocations in Thin Rods. *J. Appl. Phys.* **1953**, *24*, 176–179.

(48) Burton, W. K.; Cabrera, N.; Frank, F. C.; Mott, N. F. The growth of crystals and the equilibrium structure of their surfaces. *Philos. Trans. R. Soc. Ser. A* **1951**, *243*, 299–358.

(49) Singh, B.; Lin, H.; Prasad, R.; Bansil, A. Topological phase transition and quantum spin Hall state in TlBiS2. *J. Appl. Phys.* **2014**, *116*, 033704.

(50) Zhang, Q.; Cheng, Y.; Schwingenschlögl, U. Emergence of topological and topological crystalline phases in TlBiS2 and TlSbS2. *Sci. Rep.* **2015**, *5*, 8379.

(51) Antonius, G.; Louie, S. G. Temperature-Induced Topological Phase Transitions: Promoted versus Suppressed Nontrivial Topology. *Phys. Rev. Lett.* **2016**, *117*, 246401.

(52) Imai, T.; Chen, J.; Kato, K.; Kuroda, K.; Matsuda, T.; Kimura, A.; Miyamoto, K.; Eremeev, S. V.; Okuda, T. Experimental verification of a temperature-induced topological phase transition in $TlBiS_2$ and $TlBiSe_2$. *Phys. Rev. B* **2020**, *102*, 125151.

(53) Xu, S.-Y.; Xia, Y.; Wray, L. A.; Jia, S.; Meier, F.; Dil, J. H.; Osterwalder, J.; Slomski, B.; Bansil, A.; Lin, H.; Cava, R. J.; Hasan, M. Z. Topological Phase Transition and Texture Inversion in a Tunable Topological Insulator. *Science* **2011**, *332*, 560–564.

TOC Graphic

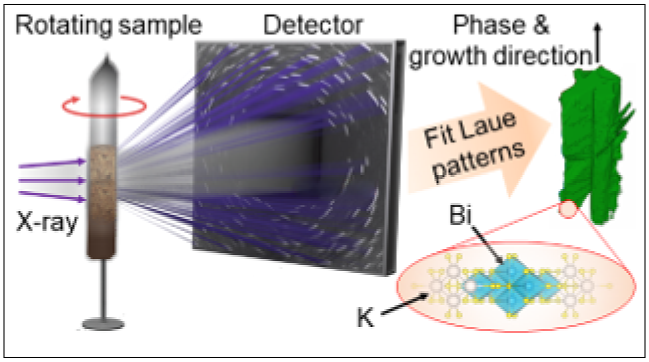
Rotating sample
Detector
Phase &
growth direction
Fit Laue patterns
X-ray
Bi
K